Coordination Chemistry Reviews 254 (2010) 2416–2428

Contents lists available at ScienceDirect

Coordination Chemistry Reviews

journal homepage: www.elsevier.com/locate/ccr

Review

Directed self-assembly of inorganic redox complexes with artificial peptide scaffolds

Carl P. Myers, Mary Elizabeth Williams*

Department of Chemistry, The Pennsylvania State University, 104 Chemistry Building, University Park, PA 16802, USA

Contents

* Corresponding author. Tel.: +1 814 865 8859; fax: +1 814 865 3292.
E-mail address: mbw@chem.psu.edu (M.E. Williams).

0010-8545/$ – see front matter
doi:10.1016/j.ccr.2010.02.018

ARTICLE INFO

Article history:
Received 2 November 2009
Accepted 15 February 2010
Available online 20 February 2010

Keywords:
Self-assembly
Oligopeptide
Peptide nucleic acid
Metal complexes
Photoinduced electron transfer
Aminoethylglycine
Redox
Electrochemistry

ABSTRACT

An ongoing challenge in the construction of supramolecular systems is controlling the relative geometry of functional redox species for molecular electronics devices, including wires, switches, and gates. This review focuses on the use of artificial peptide strands to assemble inorganic complexes that are redox active. These approaches toward macromolecular assembly use varying oligoamide backbones and assembly motifs that grew from earlier reports of single oligolysine or proline chains containing pendant redox species that undergo photoinduced charge separation. Recently, peptide nucleic acid chains that form double-stranded duplexes analogous to DNA by hydrogen bonding of complementary base pairs have been modified to contain metal complexes. In these structures, hydrogen bonding and metal coordination combine to form crosslinks between the PNA strands. Finally, a family of structures is described that is based on an aminoethylglycine scaffold with pendant metal coordination sites, but without intervening nucleic acid base pairs. These structures form multimetallic complexes that are either single- or double-stranded, or that form hairpin loop structures. These motifs for using artificial peptide strands for self-assembly hold electron donors and acceptors in relative positions that provide structural connectivity and permit electron transfers between linked metal complexes. This is a new approach for creating polyfunctional redox architectures that could ultimately enable the construction of potentially large and complex molecular electronics devices.

1. Introduction

Nature utilizes self-assembly to create macromolecules that are capable of performing the functions necessary for life. For example, photosynthetic organisms self-assemble supramolecular structures that are capable of undergoing electron transfer reactions after the absorption of a photon, leading to chemically functional charge separated states. In so doing, this multi-step process provides the necessary energy requirements to fuel biological systems. Making synthetic supramolecular analogs of biological electron transfer cascades may ultimately lead to molecular computing, photocatalysts, solar fuel production, etc. Much attention has been paid to this topic and several reviews describe approaches to this challenge that include organic [1–3] and inorganic [4–6] examples and others utilizing fullerenes and ruthenium compounds [7,8]. The synthetic challenge is to build large structures capable of long-range, sequential electron transfers that are robust and versatile. In this review, we describe tactics that, in combination, mimic two of the prevalent strategies in nature: self-assembly by molecular recognition, and the use of repeating units of amino acids to form larger peptides, proteins, and enzymes.

1.1. Synthetic mimics of biomolecules

Natural structures primarily rely on hydrogen bonding to assemble complex tertiary architectures. For example double-stranded (ds) DNA hybridizes by self-assembly using hydrogen bonding recognition of nucleic acid complements (e.g. A–T and G–C base pairing). The predominant approach in inorganic synthetic analogs is to rely on metal coordination chemistry as a means of self-assembly. For example, Hupp and coworkers self-assembled molecular squares and rectangles with Re carbonyl complex corners and symmetrical nitrogen heterocycles (e.g. 4,4′-bipyridine or pyrazine) walls [9]. This chemistry has been expanded to form assemblies with complex catalytic and photochemical properties [10–13]. Likewise, Stang and Cao have been instrumental in developing well-controlled assembly of molecular geometries using metal–ligand interactions, primarily with Pd and Pt [14]. These structures have been reported for potential applications in molecular recognition and catalysis [15–18].

Macromolecules that make up living organisms are built from repeating units. Nucleobases present in RNA and DNA along a sugar phosphate backbone with simple linkages can be arranged in any sequence and length. Like nucleic acids, proteins are comprised of amino acids; the sequence and type of modular repeating units define the function of the macromolecule. This review describes synthetic analogs that take inspiration from these, with the goal of using the versatility of modular units without the need for *de novo* synthesis of new structures. Together with metal coordination based self-assembly, polyfunctional and reconfigurable inorganic redox structures can be readily prepared.

1.2. DNA with "metallobase" pairs

Several research groups have replaced nucleic acid base pairs in duplex DNA with inorganic complexes, often called "metallobase" pairs, to produce hybrid assemblies. In this methodology, analogous to A–T and G–C Watson–Crick base pairs, ligands on opposite chains are "complementary" with respect to coordinative saturation of the metal center. For example, for a four-coordinate metal (e.g. Cu^{2+}, Zn^{2+}, or Pt^{2+}) the ligand pairs bidentate–bidentate (e.g. bipyridine–bipyridine, 2×2) or tridentate–monodentate (e.g. terpyridine–pyridine, 3×1) are complementary ligand pairs. Alternatively using octahedral metals such as Fe^{2+} or Co^{2+}, the tridentate–tridentate pair (e.g. terpyridine–terpyridine, 3×3) would be complementary.

Shionoya and coworkers designed a number of hybrid DNA systems that incorporate metal complexes into the sugar phosphate scaffold [19–23]. Meggers et al. incorporated artificial bases into DNA duplexes: in one example, dipic ligands were inserted in the oligonucleotide and Cu^{2+} formed coordinative crosslinks [24]. This structure was later crystallographically characterized as helical [25]. Additional refinements using this strategy incorporated Ag^{+} metal ions [26] and modified the backbone to glycol nucleic acid (GNA) [27]. A separate review in this issue by Shionoya describes metallobase pair modified DNA in detail.

1.3. Amino acid based structures

Amino acid building blocks provide a facile approach toward synthesizing large structures capable of performing redox processes. Polyamide backbones have the structural simplicity and programmability to synthesize a variety of structures that control the placement and identity of metal complexes and allow electronic communication between metal centers. When combined with chromophores, electron donors and acceptors, these structures can form the electron transfer cascades necessary for artificial photosynthesis. This review describes recent efforts that couple metal complexes with polyamides that ultimately will be used for the purposes of electron transfer in long-range cascades and forma-

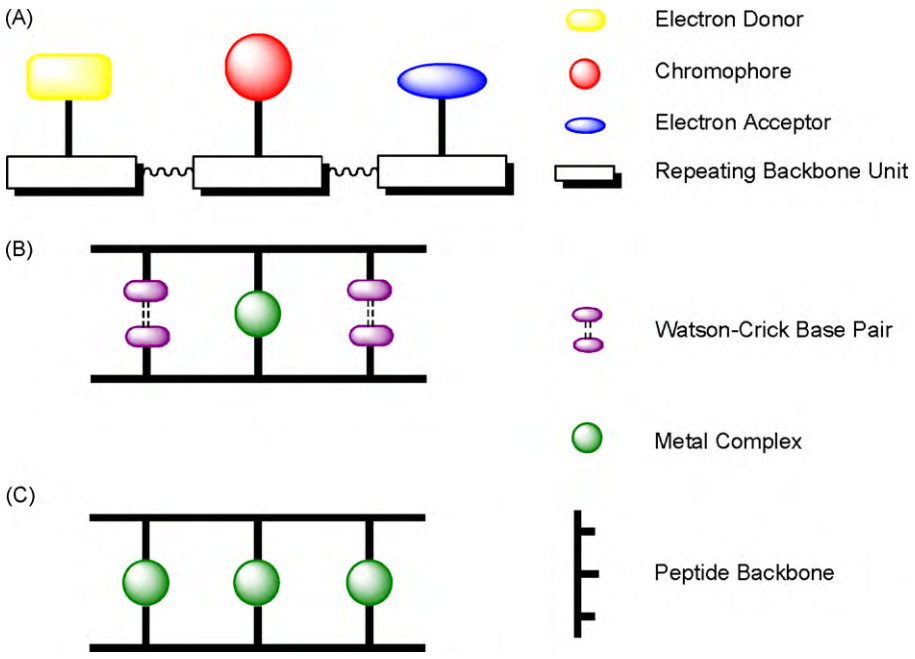

Fig. 1. Cartoon of general structures of donor–acceptor assemblies.

tion of long-lived charge separate states. We focus on structures as depicted in Fig. 1. Fig. 1A shows a linear array of donors and acceptors linked through a repeating backbone. Note that all functional components of this system stem from a single strand and are essentially on the same side. We further describe assemblies that form duplex structures either with (Fig. 1B) or without (Fig. 1C) the assistance of natural Watson–Crick base pairs.

2. Electron donors and acceptors linked by a peptide backbone

An approach for systematically synthesizing large structures of chromophores, electron donors and acceptors uses peptide coupling chemistry to arrange these in specific arrays. Several examples describing the combination of $[Ru(bpy)_3]^{2+}$ complexes with organic donors and acceptors such as anthraquinone (ANQ) and phenothiazine (PTZ) have been described and their general structures are shown in Fig. 2. These molecules have been extensively reviewed in the literature [4,5] – we briefly summarize some of the results here by way of introduction to metal complex containing oligopeptide assemblies.

2.1. Photoinduced electron transfers in substituted oligoproline chains

In initial studies of photoinitiated electron transfers in the peptide-linked donor–acceptor molecules, $[Ru(bpy)_3]^{2+}$ was linked with organic donors and acceptors by substituting a bipyridine ligand [28–31] to a lysine monomer [32–34] within a repeating lysine oligopeptide chain (Fig. 2A) [35]. Modifications of this strategy led to examples of a polysubstituted oligoproline strand, shown in Fig. 2B, in which the photophysical properties were studied [36]. In both cases, these oligopeptides were synthesized using a solid-phase resin support to afford a predetermined sequence of pendant redox species or functional groups in specific positions along the backbone. Oligoproline chains had an α-helical structure, so that careful selection of the substituted amino acid location arranged the chromophore, donor, and acceptor species on the same side of helix rod with a separation distance of ~9 Å [36,37].

By monitoring the growth and decay of peaks associated with active species in the transient absorption spectra, the mechanism of excited state relaxation was elucidated [36]. Examples of the transient absorption spectra following excitation of the Ru complex at 460 nm are shown in Fig. 3. Photoexcitation at this wavelength caused a metal to ligand charge transfer (MLCT) in the Ru complex, forming the $PTZ–Ru^{III}(bpy)_2(bpy^{-\bullet})–ANQ$ species that quickly decayed by electron transfer from PTZ → Ru to give $PTZ^{+}–Ru^{II}(bpy)_2(bpy^{-\bullet})–ANQ$. A second rapid electron transfer from $bpy^{-\bullet}$ → ANQ led to the charge separated species $PTZ^{+}–Ru^{II}(bpy)_3–ANQ^{-\bullet}$; the charge separation efficiency and lifetime were 53% and 175 ns, respectively. Monitoring the absorbance of the oxidized PTZ and reduced ANQ species, these exhibited a monoexponential decay to the ground state at the same rate, indicative of a direct electron transfer from $ANQ^{-\bullet} \rightarrow PTZ^{+}$.

To increase the charge separation efficiency using the oligoproline backbone, Meyer et al. designed and synthesized a chain that included two pendant $[Ru(bpy)_3]^{2+}$ complexes in the sequence PTZ–Ru–Ru–ANQ [38]. In comparison with the previously reported triad [36], the emission transient of the di-ruthenium containing oligoproline assembly revealed a biexponential decay with excited state lifetimes $\tau = 50$ ns and $\tau = 1120$ ns. The transient absorption spectra contained bands associated with the $Ru–bpy^{-\bullet}$ radical anion, $PTZ^{+\bullet}$ and $ANQ^{-\bullet}$. Addition of the second Ru chromophore dramatically increased the charge separation lifetime (2000 ns), however the efficiency of charge separation in this array was only ~20% [36]. Temperature-dependent studies ruled out back electron transfer via transfer to either of the Ru complexes. Additional possible relaxation pathways were Ru → Ru energy transfer and quenching of Ru^{II*} by ANQ, which were also largely ruled out because of their low relatively efficiency.

2.2. Solvent dependence of electron transfer in substituted oligoprolines

A thorough investigation of the solvent dependencies of the photodynamics in these systems was reported [39]. Using a 13-unit oligoproline, an assembly was synthesized with a 3-proline separation between PTZ and $[Ru(bpy)_3]^{2+}$ and again between the

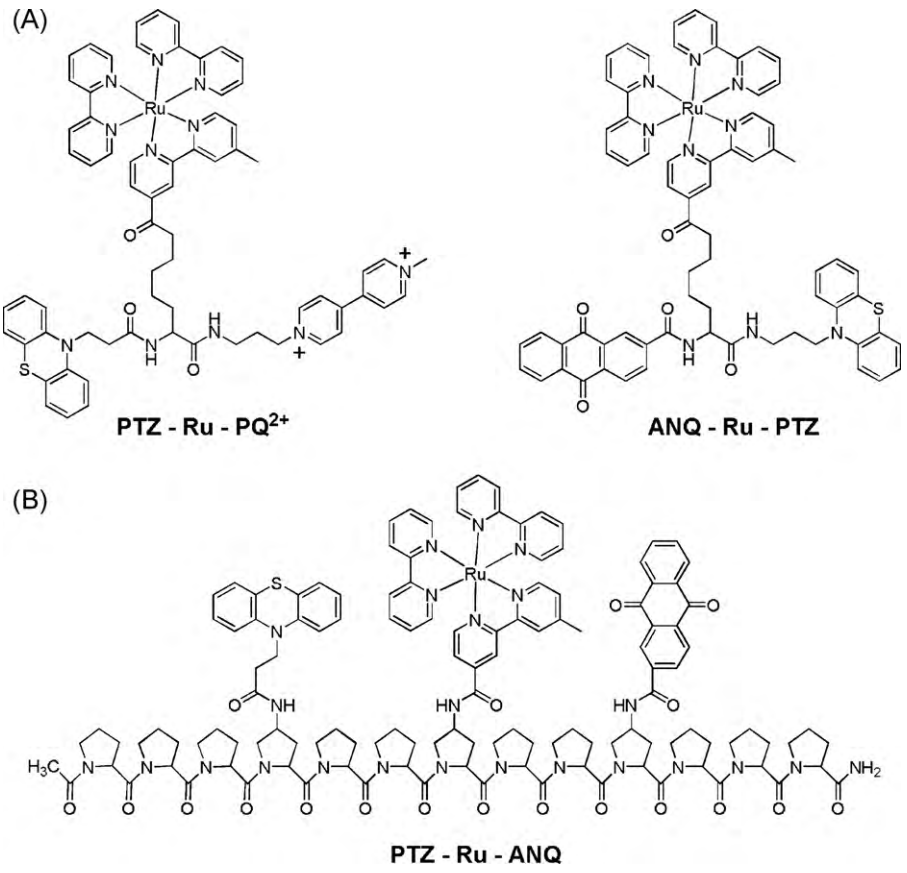

Fig. 2. Chromophore, donor, and acceptor linked by (A) oligolysine and (B) oligoproline.

Ru complex and ANQ. The photophysical and electrochemical properties of the molecule were analyzed in dichlorethane (DCE), butyronitrile (BuCN), acetonitrile (ACN), and dimethylacetamide (DMA). Based on CD spectra, the proline II helical structure was maintained in the series of solvents. Further, in all solvents, the transient absorption spectra contain bands that were attributed to the appearance of $PTZ^{+\bullet}$ and $ANQ^{-\bullet}$ at 520 and 600 nm, respectively, and the $[Ru(bpy)_3]^{2+}$ quenching time scale was 10–20 ns. Decays of these transient species were monoexponential, consistent with direct charge recombination to return to the ground state.

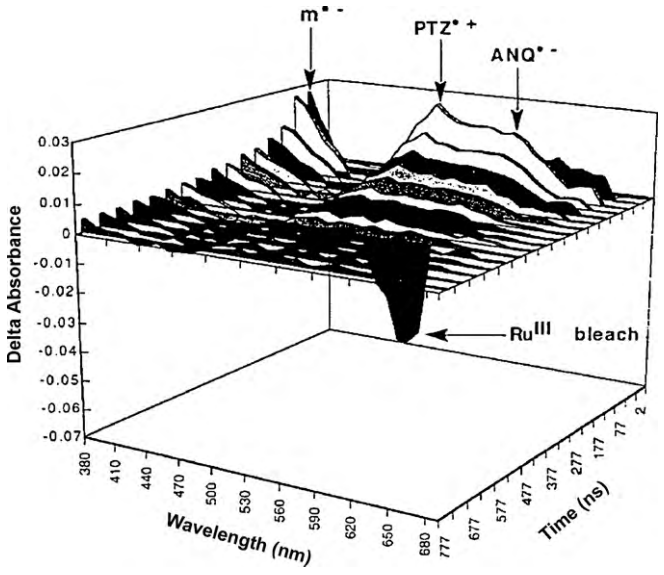

Fig. 3. Nanosecond transient absorption difference spectra for the oligoproline redox triad 1. Following a 4-ns pulse from a 460 nm laser (1.5 mJ per pulse), spectra were recorded at intervals from 2 to 777 ns for a 1.0 μM peptide triad 1 in freeze–pump thaw degassed acetonitrile at 25 °C. Reproduced with permission from Ref. [36]. Copyright (1996) National Academy of Sciences, U.S.A.

Comparison of the relative reduction potentials further supported the electron transfer mechanism. In comparison to the driving force for the $Ru^{III}(bpy)_2(bpy^{-\bullet}) \rightarrow ANQ$ electron transfer, the free energy of the $PTZ \rightarrow Ru^{III}(bpy)_2(bpy^{-\bullet})$ electron transfer quench (ΔG) is more favorable by −0.44, −0.36, −0.34, and −0.24 eV in DCE, BuCN, ACN, and DMA, respectively. Quantum yields for formation of the charge separated state were 33% in DCE, 54% in BuCN, 86% in ACN, and 43% in DMA. Based on the differences in ΔG and quenching quantum yields, a solvent-dependent competition between formation of the charge separated state $PTZ^{+\bullet}$–Ru–$ANQ^{-\bullet}$ and back electron transfer to return Ru^{II} and PTZ to the ground state was hypothesized. However, once charge separation occurred, recombination was by direct $ANQ^{-\bullet} \rightarrow PTZ^{+\bullet}$ electron transfer. Analysis of the ANQ and PTZ redox potentials showed that this highly favorable reaction occurred in the Marcus inverted region [40]. The rate of back electron transfer was solvent-dependent and occurred through-bond and/or through-space.

2.3. Mechanism of electron transfers in substituted oligoprolines

In a follow-up study, Meyer and coworkers tested through-space electron transfer mechanism in the oligoproline-based assemblies by synthesizing a series of strands with varying distances between redox species [41]. Electron transfer rate varies with solvent reorganization energy, internuclear separation, and electronic coupling between the reactive species, and the distance dependence of these varies for through-bond and through-space

interactions [42–44]. Therefore, the distance between Ru and PTZ was varied by 2, 3, 4 and 5 proline units, giving rise to variation of linear distances to 8, 20.2, 16.8, and 21.4 Å, respectively. The separation distance decreases when the number of prolines is increased from 3 to 4 because of the helical twist inherent of the oligopeptide. Using these structures, the mechanism of electron transfer for short distances (i.e. 2–4 proline units) could be through-bond but for long distance (i.e. 5 proline units), electron transfer was more likely through-space. However, analysis of the rate versus distance correlation revealed that the dominant charge separation mechanism was through-space electron transfer quenching with some contributions from through-bond electronic coupling. Conversely, the back electron transfer was dominated by singlet–singlet electron transfer. The photoinduced electron transfer pathway was complex, occurred in both the normal and inverted regions, and the reaction dynamics were largely governed by nuclear motions.

These seminal studies demonstrated that multifunctional redox assemblies could be tethered with an oligopeptide scaffold. Using this motif, charge separated states were created by photoinitiated electron transfers between the tethered donor and acceptor species. Hydrogen bonding of the oligopeptide created an alpha helical structure, with controllable and predictable distances between redox species based on the modular units of the amino acids on the backbone. These experiments were the first demonstration of using modular amino acid repeating units to control the placement of and electron transfers between inorganic species. The structures provide critical understanding for building and studying the photophysics of hybrid inorganic–organic molecules, which is now being extended to more complex architectures and assemblies and ultimately to redox cascades and molecular electronics devices.

3. Metallobases in peptide nucleic acid architectures

DNA modified with metal-binding ligands in place of natural nucleobases offers a unique motif for controlled arrangement of metal centers within a double-stranded scaffold [19–27]. Coordination of a transition metal ion by pendant and complementary ligands forms coordinative crosslinks which have been called "metallobases". Precise placement of these metal centers may enable the construction of large arrays of complexes, each contributing their unique properties toward electron transfer. To avoid the ionic interaction of metal ions with the backbone phosphates, the use of peptide nucleic acid (PNA) have instead been employed.

3.1. Inorganic complexes linked to peptide nucleic acid

Peptide nucleic acid was first designed to interact with DNA to bind into the major groove of a DNA duplex forming a triplex in solution [45]. Since that time, its dynamics as a DNA analog have been well documented and several reviews exist on the subject [46,47]. PNA is based on substitution of natural nucleic acids along an aminoethylglycine (aeg) peptide backbone that is charge neutral. Recognition between aeg strands, or between PNA and DNA, occurs through hydrogen bonding between complementary nucleic acid base pairs to form double-stranded duplexes analogous to duplex DNA. Fig. 4 shows a PNA–DNA hybrid duplex to illustrate their structural differences [46]. By virtue of the lack of electrostatic repulsion between the strands, PNA duplexes have greater stability than their ds DNA counterparts. Metal complexes that can serve as electron donors and acceptors have been incorporated into the PNA scaffold by covalently linking ligands to the secondary amines in the aeg backbone.

3.1.1. Redox-tagged PNA strands

Metzler-Nolte and coworkers developed methods to incorporate metal complexes within a PNA framework [48]: in 2002,

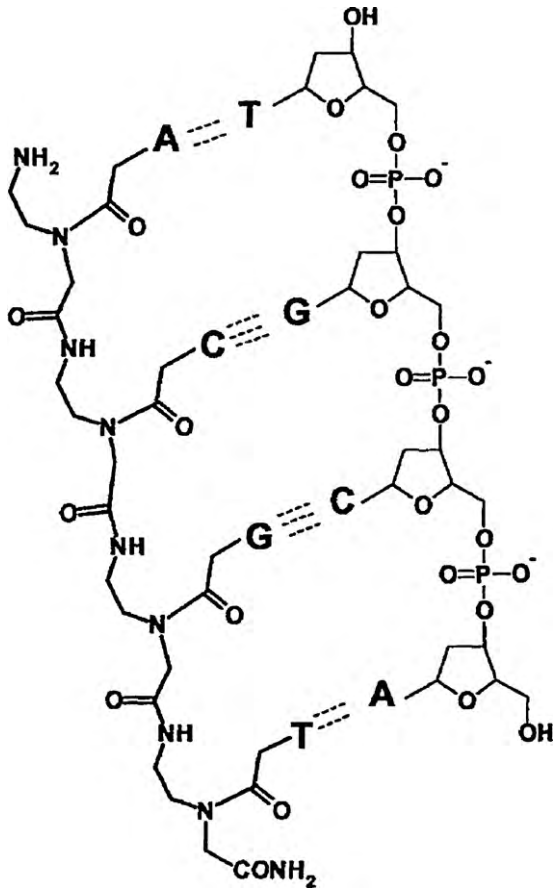

Fig. 4. Structures of DNA and PNA. A, C, G, and T are the nucleobases adenine, cytosine, guanine, and thymine, respectively. Reproduced with permission from Ref. [46]. Copyright (1997) the Royal Society of Chemistry.

$Mo(CO)_3$ was coordinated to bis(picolyl)amine (bpa) substituted PNA strands for potential use as biomolecular labels by infrared spectroscopy detection. A benefit of the bpa ligand was its ease of modification with a carboxylic acid for coupling to the free amines present in the peptides. These compounds exhibited one-electron oxidations at ~−0.25 V in acetonitrile. Electronic spectra were dominated by MLCT bands at 327 and 420 nm and extinction coefficients (ε) ranging from 6.1×10^3 to $7.0\,M^{-1}\,cm^{-1}$. Each complex also had a unique infrared CO stretching frequency ($1779–1906\,cm^{-1}$), providing spectroscopic signatures potentially useful for biomolecular labeling.

3.1.2. Electrochemical detection of DNA using redox-tagged PNA

The use of PNA in DNA detection is potentially advantageous because PNA–DNA interactions are stronger and less dependent on salt concentration. For this reason, Metzler-Nolte and coworkers synthesized a series of metallocene-functionalized PNA oligomers for direct, electrochemical detection of DNA [49]. These aeg oligopeptides were synthesized via solid-phase techniques and capped at their termini with either ferrocene (Fc) or cobaltocenium (Cc^+). A solution containing the PNA–metallocene compounds was introduced to a Au electrode surface containing a monolayer of thiol-terminated DNA. Electrochemical techniques were used to probe the hybridization of the redox-tagged PNA sequences to the DNA on the electrode surface. In the case of PNA–Fc, an oxidation wave was observed at 0.44 V which was assigned to the $Fc^{0/+}$ redox couple. Electrochemistry of the Cc^+-substituted PNA analog, with a more rigid linker, revealed a reduction peak at −0.92 V when hybridized to the surface. These are the first descriptions of electro-

chemical experiments using redox-active inorganic modified PNA structures.

3.1.3. Click chemistry for tagging PNA with redox probes

These early studies demonstrated linking redox-active species to the PNA scaffold. Since that initial report, more sophisticated techniques for metallocene addition to peptides have been developed. Using a Cu(I) catalyst, Metzler-Nolte et al. utilized [3 + 2] dipolar cycloaddition, or "click" chemistry, to link Fc complexes derivatized with terminal azides to react with peptide chains containing alkynes [50]. This chemistry was recently expanded to create a library of Fc-based peptide structures with varying oxidation potentials based on electronic substituents pendant from the Fc cyclopentadienyl ring [51].

3.2. Metallobases in PNA duplexes

The first example of a ligand-modified duplex PNA structure for coordination of a metal ion to form a metallobase crosslink was described by Achim and coworkers [52]. A bipyridine (bpy) derivative, 5-acetic acid-5′-methyl-2,2′-bipyridine, was inserted into two complementary PNA strands using coupling reagents and solid-phase synthesis. The ligand was placed in the center of each strand in the 10-base pair sequences:

$$\text{H-GTAG}\mathbf{M}\text{TCACT-Lys}\text{NH}_2$$

$$\text{H}_2\text{N-Lys-CATC}\mathbf{N}\text{AGTGA-H}$$

where M = N = bpy. These were purified by HPLC and characterized by MALDI-TOF mass spectrometry.

3.2.1. Metal binding in ligand-containing PNA duplexes

It is known that bpy forms the square planar complexes $[Ni(bpy)_2]^{2+}$, $[Pd(bpy)_2]^{2+}$, and $[Pt(bpy)_2]^{2+}$; addition of these transition metal ions coordinatively crosslinked the bpy-substituted PNA strands. Following hybridization to form the PNA duplex by complementary base pairing, circular dichroism (CD) was used to monitor metal binding in the duplex PNA structure. These data showed that both with and without Ni^{2+}, the single strand complements form double-stranded duplex structures.

Melting temperatures (T_m) were measured to determine the stability of PNA duplexes: in fully complementary duplexes, T_m was 66.5 °C and base pair mismatches led to a destabilization by ~15–16 °C. Substitution of one of the nucleic acid base pairs with bpy ligands led to a decrease in T_m by 16–19 °C. However after addition of Ni^{2+} to this duplex, T_m increased to 59 °C. This result indicated both an increase in stability for the duplex (compared to unmatched) and coordination of Ni^{2+} by the free bpy ligands. No effect on melting temperature was observed after the addition of $K_2[PdCl_4]$ or $K_2[PtCl_4]$.

3.2.2. Hydroxyquinoline–metallobase PNA duplexes

The lower T_m in the metal-linked PNA duplex versus the fully complementary PNA structure may have been due to slight destabilization of the base pairs adjacent to the Ni complex through disruption of their hydrogen bonding or π-stacking ability. Steric hindrance prevented $[Ni(bpy)_2]^{2+}$ from adopting a planar geometry, and forced it into a slightly distorted square planar which could have effected the nearby base pairs. To test this assumption, Achim et al. incorporated 8-hydroxyquinoline (HQ) into the PNA scaffold [53]. This ligand readily formed square planar complexes with Cu^{2+} to give $[Cu(HQ)_2]$ and had previously been used in synthetic DNA analog scaffolds to greatly increase duplex stability [27].

Several variations of 10-bp complementary PNA strands were synthesized, substituted with and without a single HQ ligand at defined positions. In the absence of Cu^{2+} in solution, the melting temperature of HQ-substituted PNA was 21 °C less than unsubstituted (fully complementary) PNA. However, after the addition of 1 equiv. of Cu^{2+}, T_m increased by >33 °C, higher than the fully complementary PNA duplex. An interesting finding was that the Cu^{2+} bound sufficiently strongly to the HQ ligands that this occurred even in the presence of nucleic acid base pair mismatches. However in the absence of any Watson–Crick base pairs, PNA duplexes did not form by metal coordination alone. EPR and UV–vis titrations were used to confirm the presence of $[Cu(HQ)_2]$ and their square planar geometry. The EPR spectra suggested that both *cis*- and *trans*-isomers of the $[Cu(HQ)_2]$ complex form within the PNA duplex, and that small solvent molecules were not coordinated in the axial positions.

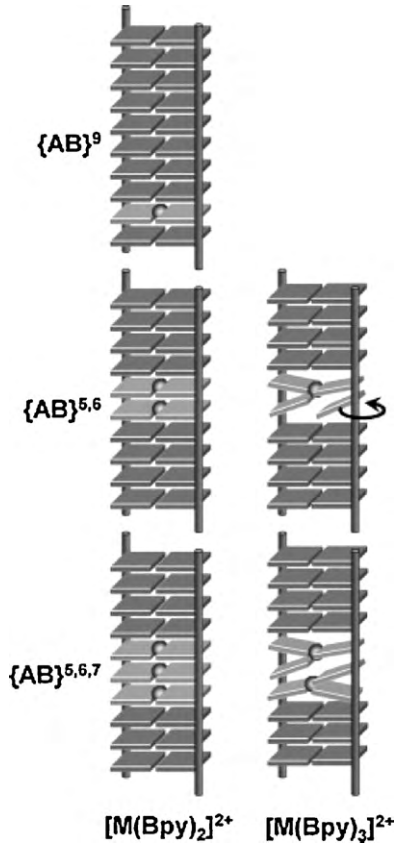

Fig. 5. Cartoon representations of possible structures of metal–bpy containing PNA Duplexes. Reproduced with permission from Ref. [54]. Copyright (2006) the American Chemical Society.

3.2.3. Variation of position and number of metallobases in PNA duplexes

The position and number of metal complexes within the duplex were significant in determining the global properties of the structure. In detailed studies of these effects [54], Cu^{2+} and Co^{2+} were added to bpy-modified 10-bp PNA duplexes containing 1–3 sets of bpy ligand pairs. Further, the positions of these along the PNA backbone were varied to determine the effect of metallobase position within the scaffold. Fig. 5 shows a cartoon of the possible structures used in this study.

Placement of the bpy ligand pair at the end of the PNA duplex resulted in a T_m that was essentially the same as an unmodified PNA duplex. This is in stark contrast to previous work [53] with bpy ligands in the center of the PNA duplex, and resulted from "fraying" in the ends of the peptide strand. These researchers fur-

ther determined that increasing the number of bpy substitutions within the PNA duplex led to a decrease in overall stability (i.e. lower T_m). Addition of the metal ions Ni^{2+}, Co^{2+}, and Cu^{2+} to PNA sequences containing a single bpy ligand pair in the center of the duplex caused stabilization of the duplex by +14 °C, +6 °C, and +4 °C, respectively. This trend reflected larger binding affinity of bpy for Ni^{2+}. However, when the bpy ligands were placed at the end of the PNA chains, addition of metal ions had a greater effect on stabilization of the duplex:Ni^{2+}, Co^{2+} and Cu^{2+} increased T_m by +20 °C, +13 °C, and +10 °C, respectively, which was attributed to linking the frayed ends of the duplex.

When two pairs of bpy ligands were inserted into the PNA duplex, addition of 2 equiv. of Ni^{2+} raised the melting temperature to 45 °C, +9 °C higher than the unmetallated form. However, this melting point is lower than in PNA duplexes containing a single Ni metallobase (T_m = 57 °C), suggesting lower stability. The authors hypothesized that addition of the second metal caused a decrease in stability because of repulsion of the charged metal centers within the duplex. It was also possible that a single PNA strand containing four metal binding sites coordinated to a single Ni^{2+} atom before duplex formation occurs.

By monitoring changes in the $\pi \rightarrow \pi^*$ region in the spectrum, UV–vis titrations of the addition of Ni^{2+} or Cu^{2+} to the PNA sequences containing a single pair of bpy ligands revealed a 1:1 coordination stoichiometry. Titrations with PNA sequences containing two sets of bpy ligands revealed a 1:1 ratio for Ni^{2+} titrations, not the 2:1 that would be expected for the formation of two adjacent $[Ni(bpy)_2]^{2+}$ complexes. Analogous observations were made using Cu^{2+}, suggesting that each metal ion formed a $[M(bpy)_3]^{2+}$ complex within the PNA duplex structure, leaving a single uncoordinated bpy ligand (Fig. 5). At higher metal concentrations, very small inflection points in the titration curve pointed toward a conversion to two $[M(bpy)_2]^{2+}$ complexes.

Titrations with a PNA sequence containing three bpy ligand sets showed an increase in absorbance between 300 and 320 nm as a result of changes in the $\pi \rightarrow \pi^*$ transition. Spectrophotometric titrations with Ni^{2+} and Cu^{2+} resulted in titration curves that reached a plateau at a stoichiometry of 2:1 metal ion per PNA duplex, suggestive of the formation of two $[M(bpy)_3]^{2+}$ complexes. At high metal ion concentrations, there again existed a slight inflection point at 3:1 Ni^{2+}:duplex, indicating the transformation of two $[Ni(bpy)_3]^{2+}$ complexes into three $[Ni(bpy)_2]^{2+}$ complex crosslinks in the PNA duplex.

Copper-linked PNA duplexes were also investigated using EPR spectroscopy. In duplexes containing two and three bpy ligand sets, and respectively 1 and 2 equiv. of Cu^{2+}, the EPR spectra were consistent with formation of $[Cu(bpy)_2]^{2+}$ and $[Cu(bpy)_3]^{2+}$ metallobase crosslinks. These data, compared with UV–vis titrations, suggested the existence of $[Cu(bpy)_3]^{2+}$ in each of the samples. However, broadening of the EPR spectra made conclusive analysis difficult: line broadening could have resulted from slight binding of the metal with nearby base pairs, the presence of a mixture of structures within the sample, or from slight coupling between the metal centers. The latter of these was dismissed based on large M–M distance within the PNA duplexes.

3.2.4. Electrochemistry of Fc-modified PNA monolayers on Au electrodes

In an effort to understand the role of charge transport (CT) in single-stranded PNA, Achim and coworkers synthesized a series of single-stranded PNA strands containing only thymine (n = 3–7). The C-terminus was modified with cysteine and the N-terminus contained ferrocene (Fc) as the redox probe [55]. When these compounds were exposed to an Au electrode surface, self-assembled monolayers (SAMs) formed. Fig. 6 shows an example structure of these species and their relative packing on a monolayer surface.

Fig. 6B shows a cartoon of the two major orientations of the Fc–thymine PNA strands on the electrode surface. At low surface coverages, many of the PNA oligomers laid flat on the surface, resulting in a small electrode–Fc separation distance. Conversely, at high surface coverages, more of the PNA strands oriented perpendicular to the surface maximizing the distance between the electrode and Fc-terminus. During an electrochemical experiment, the measured current would thus be the average of oligomers in a range of orientations relative to the electrode surface. To selectively address only the oligomers oriented perpendicular to the surface, the potential was scanned from 0.35 to 0.65 V in a 1 M NaCl solution at a scan rate of 1–10 V/s. As a result, redox silent Fe–Cl species were formed by displacement of a Cp ring. Species lying flat on the surface were preferentially destroyed because of their proximity to the electrode and fast scan rate, as evidenced by a disappearance of their contribution to the current.

Monitoring the oxidation peak maxima as a function of the scan rate allowed the determination of the heterogeneous electron transfer rate constant (k^0) for the series of oligomers as a function of length of the PNA strand: as the number of thymines increased from 3 to 7, k^0 decreased from 2000 to 0.018 s^{-1}. Plotting the rate constant versus the electron transfer distance [56,57], the tunneling decay constant was β = 0.86 $Å^{-1}$ (3.0/base). The maximum electron transfer rate constant (i.e. at r^o) was 5.8×10^8 s^{-1}, which is slower than in double-stranded DNA, but could have been because of an absence in base stacking in the single-stranded PNA.

The experiments described above lay the groundwork for future PNA–DNA hybrids for use in molecular electronics: although it has not yet been demonstrated in the metal-linked PNA duplexes, several groups have described electron transfer through double-stranded DNA duplexes and the potential for use in molecular electronics [58–63]. By analogy, the PNA-based systems could be applied to create molecular circuitry, for example by coupling electron donors and acceptors to the strand termini and between the strands to form molecular wires. The initial report discussed above provided the foundation for ultimate application in electronic devices, and demonstrated that charge transport through the PNA strands is indeed possible.

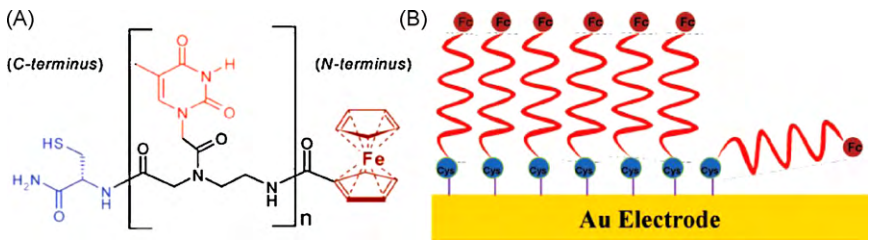

Fig. 6. (A) Chemical structure of thymine containing ss PNA that has a C-terminus cysteine and an N-terminus ferrocene, where n = 3–7. (B) Shows a schematic representation of PNA molecules self-assembled on a gold surface, in which the blue circle represents cysteine, the red curl represents PNA, and the light brown circle represents ferrocene. Reproduced with permission from Ref. [55]. Copyright (2008) the American Chemical Society.

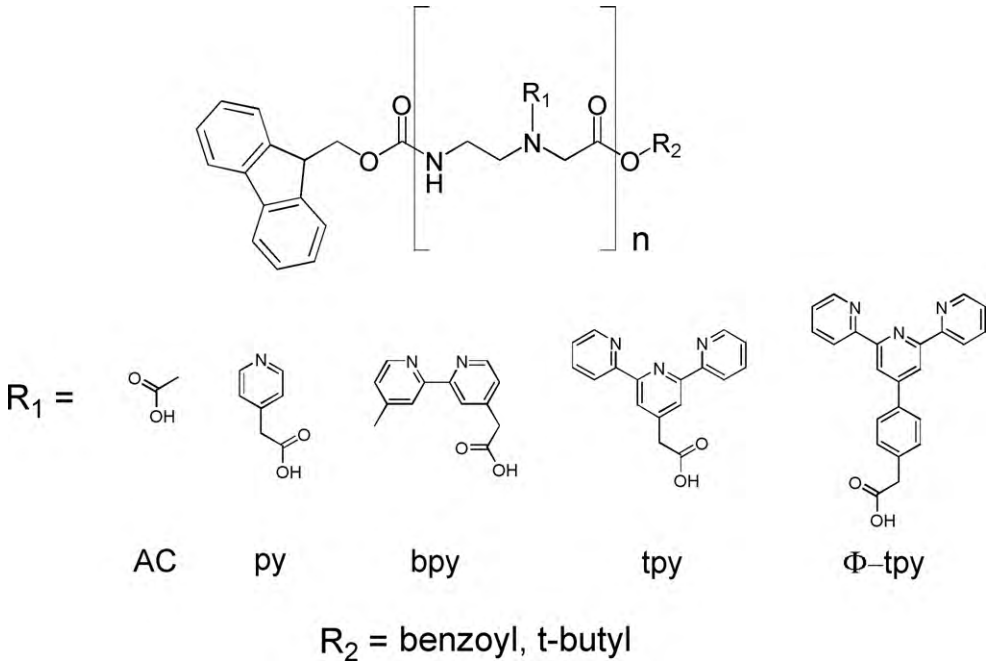

Fig. 7. Structure of aminoethylglycine (aeg) oligopeptide with pendant substitutions acetyl (AC), pyridine (py), bipyridine (bpy), terpyridine (tpy), and phenyl-terpyridine (Φ-tpy). R groups are linked via amide coupling through the acetic acid (n = 1–10).

4. Metal coordination based assembly of artificial peptides

Using the scaffold of duplex DNA and PNA to form a redox cascade for long-range electron transfer is somewhat restricted because of the electrochemically irreversible electrochemistry of the nucleic acids. Eliminating nucleic acids and utilizing *only* metal–ligand interaction (as in Fig. 1C) between polyamide strands is a facile approach that resolves the issues of metal binding to nucleobases and backbone phosphates, and furthermore excludes base pairs' undesirable electrochemical properties. Supramolecular systems have recently been reported that use metal complexes to crosslink artificial peptide strands without the assistance of nucleic acid pairing. In these structures, the metal complexes bind to ligands that decorate the oligopeptide chains, and in some cases form coordinative crosslinks (i.e. metallobases) between two strands, forming duplex and hairpin structures [64–71].

4.1. Ligand-substituted aeg oligopeptides

Oligomers have been built from an aeg backbone containing only pendant ligands which coordinate metal ions. Examples of this class of compounds and the ligands used are shown in Fig. 7. The ligands were chosen for their denticity and resulting metal complex product, and typically use the nitrogen donor ligands pyridine (py), bipyridine (bpy), terpyridine (tpy), and phenyl-terpyridine (Φ-tpy). Formation of multimetallic structures using the substituted oligopeptide strands has been based on the 1×3, 2×2 and 3×3 molecular recognition motifs described above.

4.1.1. Ligand-substituted monomer synthesis

First reported in 2005 [64], an aminoethylglycine (aeg) backbone was synthesized with the pendant ligands pyridine or bipyridine. Monomers were synthesized by amide coupling an acetic acid derivative of the appropriate ligand using standard reagents (e.g. HOBT, HBTU, EDC, DIPEA, etc.) to an Fmoc-protected (N-terminus) and t-butyl-protected (C-terminus) aeg unit. Yields ranged from 30 to 60% for ligand-substituted monomer syntheses. After this, either the t-butyl or Fmoc group was cleaved to yield the primary carboxylic acid or amine terminus, respectively, making these available for chain extension via additional amide coupling reactions.

Oligopeptides were synthesized on solid-phase supports using Fmoc–PAL–PEG–PS resin and, once cleaved from the resin, the products were purified by HPLC. Products yields were limited by the loading on the resin and in some cases this method afforded only very low compound yields (<5 mg). A pyridine hexapeptide (e.g. six pendant py ligands on the strand, Fmoc–(py aeg)$_6$) and bipyridine tripeptide (e.g. three pendant bpy ligands, Fmoc–(bpy aeg)$_3$) were characterized by ^{1}H NMR spectroscopy and mass spectrometry to confirm their purity and identity.

4.1.2. Coordination of four-coordinate metals to single-strand ligand-substituted aeg oligopeptides

During spectrophotometric titration, reaction of Fmoc–(py aeg)$_6$ with [Cu(pda)H$_2$O] (pda = pyridine dicarboxylic acid) showed stoichiometric binding of 6 equiv. of Cu to form six [Cu(pda)(py)] complexes tethered along the hexapeptide backbone. High resolution mass spectrometry confirmed the identity of the hexametallated product. Similarly, [Cu(tpy)(H$_2$O)]$^{2+}$ was also titrated against the Fmoc–(py aeg)$_6$ hexamer, resulting in binding of six [Cu(tpy)(py)]$^{2+}$ complexes on the backbone. This result suggested that electrostatic repulsions did not significantly affect stoichiometric metal coordination and assembly along the aeg scaffold.

Molecular modeling provided insight to the solution-phase structures of these multimetallic species. In the case of the [Cu(pda)(py)] containing Fmoc–(py aeg)$_6$ hexamer, the neutral charge allowed π-stacking of adjacent metal complexes. Modeling predicted a metal–metal distance of ~4 Å and a helical pitch of 16–17 Å. However, models of the [Cu(tpy)(py)]$^{2+}$-containing hexapeptide showed an average metal–metal distance of about 20 Å due to electrostatic repulsion of the metal complexes.

The solution structure models were supported by analysis of their EPR spectra. The [Cu(tpy)(py)]$^{2+}$ decorated hexapeptide had an EPR spectrum with a classic line shape ($g_{||}$ = 2.28; $g_{\perp}$ = 2.06; $A_{||}$ = 167 × 10^4 cm^{-1}) that was similar to a monometallic Cu complex. This result implied that each Cu complex on the aeg scaffold

was electronically identical, noninteracting (i.e. separated by at least 6 Å), consistent with the electrostatic repulsion expected in the model. In contrast, the EPR spectrum of the [Cu(pda)(py)] substituted hexapeptide had significantly broadened lines and there was a decrease in the hyperfine coupling ($g_{||} = 2.35$; $g^{\perp} = 2.09$; $A_{||} = 130 \times 10^4\ cm^{-1}$), implying weakly interacting Cu complexes and delocalization of unpaired electrons.

4.1.3. Variation of the number and type of complexes in pyridine-substituted oligopeptides

The synthesis of a series of aeg oligopeptides of varying length that contained up to 10 pendant pyridine ligands was also reported [65]. These species were synthesized on solid-phase support and characterized by NMR, mass spectrometry and pH titrations to further confirm the number of free pyridine ligands per aeg strand. Reaction of the free pyridine ligands with $[Cu(tpy)(H_2O)]^{2+}$, $[Cu(pda)(H_2O)]$, and $[Pt(tpy)(H_2O)]^{2+}$ afforded a series of peptide strands with $[M(tpy)(py)]^{2+}$ or [M(pda)(py)] complexes tethered to the backbone.

UV–vis spectrophotometric titrations of metal complexes with the py-substituted oligopeptides provided binding stoichiometries that agreed well with the number of pendant py ligands. An interesting finding during the titrations was that the same binding stoichiometry was observed when using either $[M(tpy)(H_2O)]^{2+}$ or $[M(pda)(H_2O)]$, even when using oligopeptides with as many as 10 monomer units. Since electrostatic repulsion between $[M(tpy)(py)]^{2+}$ centers could hinder subsequent binding of additional complexes, the observed stoichiometries showed that this was not the case.

Oligopeptides containing pendant $[Pt(tpy)(py)]^{2+}$ complexes offered the opportunity for electrochemical investigations. Cyclic voltammograms of these multimetallic structures contained two sequential, one-electron, reversible waves at formal potentials −0.6 and −1.1 V versus SCE that were attributed to tpy-centered reductions. No evidence of adsorption to the electrode surface was observed, even for the largest decapeptide which, when fully oxidized, had a total charge of +20 because of the 10 pendant Pt complexes. The electrochemical data were consistent with Pt complexes with independent electronic behavior as a result of electrostatic repulsion between the +2 charged species. Chronoamperometric experiments provided direct measure of the molecules' diffusion coefficients, which were related to the structures' hydrodynamic radii with the Stokes–Einstein equation.

4.2. Metal coordination based crosslinking of bpy-substituted aeg tripeptides

The bipyridine tripeptide (Fmoc–(bpy aeg)$_3$) contained three pendant bipyridine ligands available for metal coordination and as such, spectrophotometric titrations using Fe^{2+} and Cu^{2+} were (separately) evaluated. Addition of Fe^{2+} resulted in the formation of an absorbance band centered at 540 nm, consistent with MLCT transition of the $[Fe(bpy)_3]^{2+}$ complex. This band increased in absorbance and reached a maximum at ∼1:1 molar equivalence of Fe^{2+}:bpy tripeptide. Analysis by mass spectrometry revealed the molecular ion peak for the species consisting of two bipyridine tripeptides crosslinked by two Fe^{2+} centers. This result implied the formation of two $[Fe(bpy)_3]^{2+}$ complexes crosslinking the two tripeptide strands.

Separate reaction of the tripeptide with Cu^{2+} resulted in a spectrophotometrically observed equivalence point of ∼1.6 Cu:peptide. Together with mass spectrometry, this led to the conclusion that two tripeptide strands were crosslinked by three Cu^{2+} ions, forming three $[Cu(bpy)_2]^{2+}$ coordinative crosslinks. These compounds marked for the first time oligopeptide duplex self-assembly *without* the assistance of nucleic acid base pairs.

4.3. Heterometallic structures tethered by aeg oligopeptides

In the first demonstration of using the artificial aeg oligopeptides to prepare heterometallic complexes, structures containing combinations of Pt^{2+} and Cu^{2+} with Fe^{2+}, Cu^{2+}, and Zn^{2+} were evaluated [66]. This study demonstrated a synthetic technique in which peptides were grown outwardly from a central backbone unit rather than from a solid resin bead. The resulting tripeptide contained the ligand sequence py–bpy–py. Using the varying denticity of the ligands, the oligopeptide was sequentially reacted with $[Cu(tpy)(H_2O)]^{2+}$ or $[Pt(tpy)(H_2O)]^{2+}$ followed by Fe^{2+}, Cu^{2+} or Zn^{2+} ions. The former of these were used to bind to the pendant py ligands, whereas the free metal ions formed either $[M(bpy)_2]^{2+}$ or $[M(bpy)_3]^{2+}$ complexes, crosslinking two or three peptide strands, respectively. Spectrophotometric and electrochemical data were consistent with the formation of the multi-heterometallic structures.

4.4. Octahedral metal complex crosslinks in Φ-tpy-substituted oligopeptides

To be able to incorporate octahedral metal coordinative crosslinks, a series of Φ-tpy-substituted oligopeptides with lengths ranging from one to four monomers was synthesized [67]. The oligopeptides were characterized using temperature-dependent NMR spectroscopy, which provided information about the complex solution-phase structure and dynamics. Although the complexity of the NMR spectra increased as the oligopeptide length increased, full proton assignments were made using the two dimensional techniques HMQC and COSY.

4.4.1. Metal crosslinking of tpy-substituted oligopeptides

The oligopeptides were used to coordinate Co^{2+} and Fe^{2+} ions, giving $[M(\Phi\text{-tpy})_2]^{2+}$ complex crosslinked structures whose spectroscopic and electrochemical properties were compared [67]. Spectrophotometric titrations, such as those shown in Fig. 8, were used to assess the coordination of the metal ions. When monitoring the wavelength for the MLCT transition of the $[M(\Phi\text{-tpy})_2]^{2+}$ complex for both the Co^{2+} and Fe^{2+} titrations, the MLCT band increased and leveled at a finite absorbance. As seen in the titration curves in Fig. 8, the absorbance leveled at stoichiometric ratios of metal to oligopeptide duplex that indicated the major titration product was dictated by the number of ligands per peptide, and consistent with the $[M(\Phi\text{-tpy})_2]^{2+}$ crosslinked peptide duplexes. Molecular ion peaks observed in the mass spectra of these were consistent with structures in which two oligopeptides were crosslinked by $[M(\Phi\text{-tpy})_2]^{2+}$ complexes: in each case, peptides containing one, two, three, or four free Φ-tpy ligands bound one, two, three, or four metal ions.

Electrochemistry was used to further confirm solution structure and differentiate between crosslinked duplexes and coordination polymers. In the cyclic voltammetry of both the Fe- and Co-linked oligopeptide duplexes, redox couples corresponding to the $Fe^{III/II}$ and $Co^{III/II}$ oxidation were observed at 0.99 and 0.27 V, respectively. Evaluation of the oxidative waves using chronocoulometry provided measurements of the solution diffusion coefficients (D) of the complexes, which decreased with increasing peptide length. The linearity of this relationship indicated that the major species in solution were the metal-linked oligopeptide duplexes and not coordination polymers. Although these experiments did not conclusively eliminate the possibility of alternative registers and polymer formation, they suggested that the majority of species in solution were duplexes and other structures were below the experimental limits of detection.

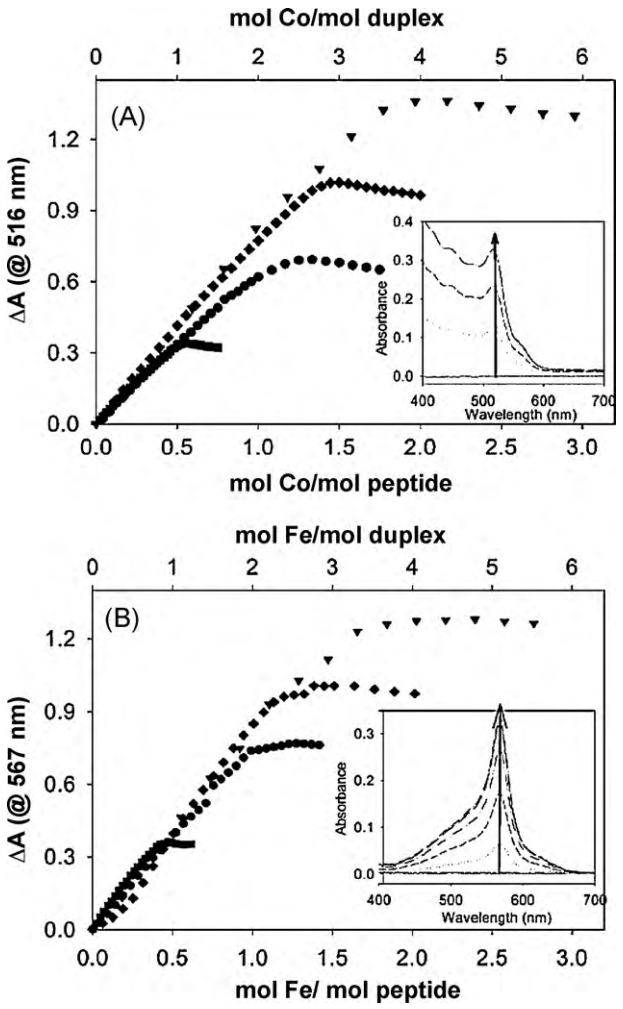

Fig. 8. Titration curves for the changes in absorbance upon addition of oligopeptide to (A) Co(II) at 514 nm and (B) Fe(II) at 567 nm for oligopeptides (■) Φ-tpy aeg monopeptide, (●) $(\Phi\text{-tpy aeg})_2$ dipeptide, (♦) $(\Phi\text{-tpy aeg})_3$ tripeptide, and (▼) $(\Phi\text{-tpy aeg})_4$ tetrapeptide in methanolic solutions. Insets show representative absorbance differences for spectra acquired during titration with $(\Phi\text{-tpy aeg})_3$ tripeptide. Reproduced with permission from Ref. [67]. Copyright (2007) the American Chemical Society.

4.4.2. Thin film electrochemistry of metal-linked Φ-tpy oligopeptides

The $[Fe(\Phi\text{-tpy})_2]^{2+}$ and $[Co(\Phi\text{-tpy})_2]^{2+}$ crosslinked oligopeptides were deposited onto Pt electrode surfaces by cycling the potential through the oxidative wave, which caused the peak current to incrementally increase. An example of these cyclic voltammograms is shown in Fig. 9A, and shows sequential cycles of an $[Fe(\Phi\text{-tpy})_2]^{2+}$ dipeptide duplex, during which the molecule is adsorbed to the electrode. The surface layer thickness was controlled by selecting the number of sequential scans; depending on the oligopeptide length, the maximum surface coverages ranged from ~4 to 22×10^{11} molecules/cm^2. After deposition, the electrode was rinsed and placed in a solution containing only electrolyte. The adsorbed peptides remained on the electrode surface even through many cycles, as shown in Fig. 9B.

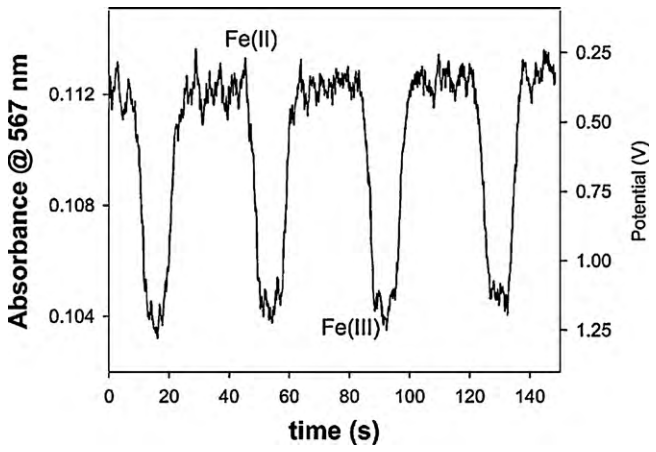

Fig. 10. Absorbance at 567 nm for a film of $[Fe_3((\Phi\text{-tpy aeg})_3)_2]^{6+}$ on ITO-coated glass in 0.2 M TBAP in ACN as the potential is swept from 0.35 to 1.35 V at 50 mV s^{-1}. Reproduced with permission from Ref. [67]. Copyright (2007) the American Chemical Society.

4.4.3. Spectroelectrochemistry of Fe-linked Φ-tpy oligopeptide duplexes

The films were further studied using spectroelectrochemistry, for which the metal-containing oligopeptides were deposited on the surface of an indium tin oxide (ITO) coated glass electrode. A potential scan was applied to deposit the peptide to the surface, after which the electrode was rinsed and placed in an electrolyte solution. The absorbance of the film at 567 nm was monitored as a function of time as the applied potential was switched between oxidative and reductive potentials (0.35 and 1.35 V). Fig. 10 shows a plot of absorbance at 567 nm versus time as the potential of the ITO electrode is switched, and illustrates the reversible nature of the $Fe^{III/II}$ reaction. The consistent return to the baseline absorbance during this experiment confirmed that the metal-linked peptide

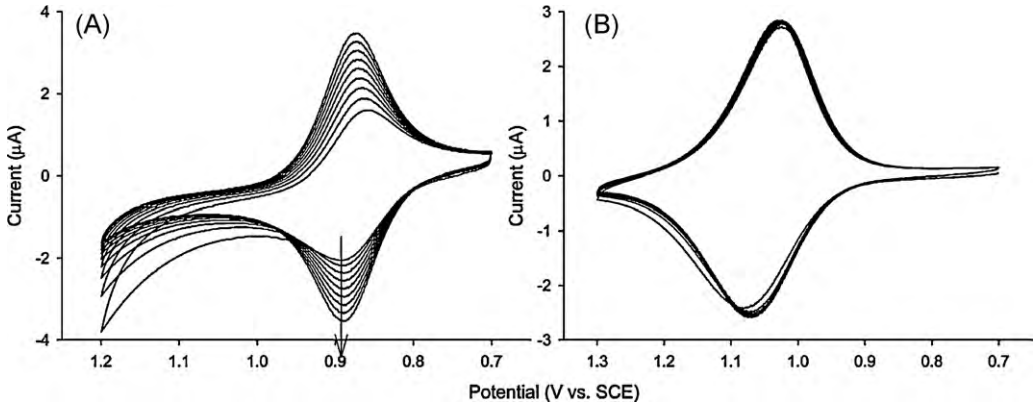

Fig. 9. (A) Sequential cyclic voltammograms of $[Fe_4((\Phi\text{-tpy aeg})_4)_2]^{8+}$ using a Pt electrode and a potential scan rate of 50 mV s^{-1}. (B) Cyclic voltammogram of the same film in 0.2 M TBAP in ACN using a scan rate of 50 mV s^{-1}. Reproduced with permission from Ref. [67]. Copyright (2007) the American Chemical Society.

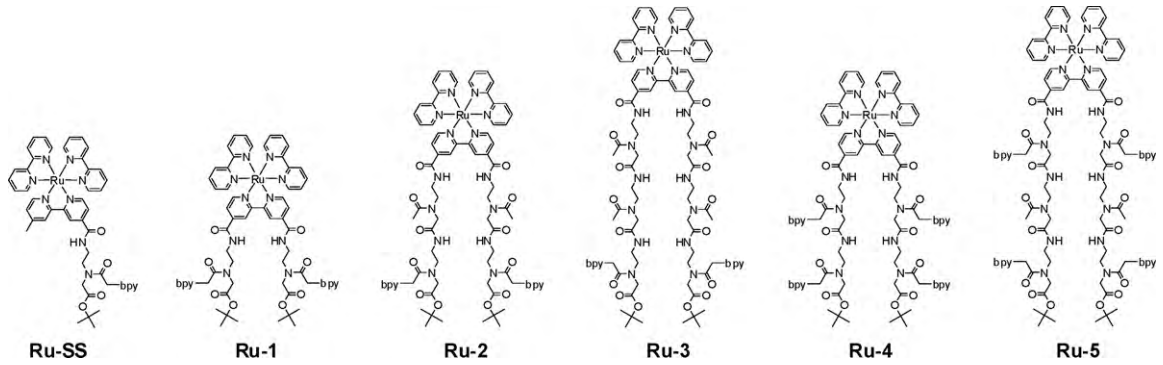

Fig. 11. Structures of $[Ru(bpy)_3]^{2+}$ single strand and hairpin complexes.

remained adhered to and did not diffuse away from the electrode surface. Furthermore, the process of oxidation did not degrade the peptide or cause new electrochemical waves to appear in the CV (e.g. the reaction is chemically reversible). In total, these experiments demonstrated the robust nature and electroactivity of the metal-bis-Φ-terpyridine crosslinked oligopeptides.

4.5. Photoinduced electron transfers in metallated aeg oligopeptides

Compounds containing $[Ru(bpy)_3]^{2+}$ moieties are promising candidates for artificial photosynthesis and photocatalysis [72–75]. In addition to having strong absorbance and emission bands in the visible region of the spectrum, following excitation at the MLCT, the long-lived triplet excited state (>1 μs) and reversible oxidation and reduction reactions offer favorable conditions for electron donation according to the reactions:

$$[Ru^{II}(bpy)_3]^{2+} + h\nu \rightarrow [Ru^{III}(bpy)_2(bpy^{-\bullet})]^{2+} \quad (1)$$

$$[Ru^{III}(bpy)_2(bpy^{-\bullet})]^{2+} + A \rightarrow [Ru^{III}(bpy)_3]^{3+} + A^{-\bullet} \quad (2)$$

$$[Ru^{III}(bpy)_2(bpy^{-\bullet})]^{2+} + D \rightarrow [Ru^{II}(bpy)_2(bpy^{-\bullet})]^{+} + D^{+} \quad (3)$$

where A is an electron acceptor and D is an electron donor.

4.5.1. Single strand aeg-substituted Ru complexes

A $[Ru(bpy)_3]^{2+}$ center was substituted with a single aeg strand containing a free bpy ligand [68] as shown in Fig. 11 (**Ru**–**SS**). Characterization of this compound revealed a long-lived 1.42 μs excited state lifetime and a quantum yield of 4.3%. When Cu^{2+} was added to a solution containing a known molar amount of the **Ru**–**SS** complex, the emission intensity decreased and leveled at roughly 1:2 Cu:Ru, suggesting that a single Cu^{2+} atom bound two $[Ru(bpy)_3]^{2+}$ centers by formation of a $[Cu(bpy)_2]^{2+}$ complex. Elemental analysis was consistent with the Cu-linked di-ruthenium species.

4.5.2. Inorganic analogs of nucleic acid hairpins using aeg-substituted aeg oligopeptides

One of the major challenges inherent to using the ligand-substituted oligopeptides without nucleic acid base pairing to guide orientation and prealignment is the possibility of forming isomers, as illustrated in Fig. 12. For example, for a bipyridine dipeptide both parallel and antiparallel alignments are possible. In addition, misalignment leading to polymer formation can occur. To discourage this, the structural motif shown in Fig. 12C was designed and synthesized [68,71]. In the first example of this, two complementary bipyridine-substituted aeg strands were attached to a single bridging unit, the 4- and 4′-positions of a bipyridine ligand coordinated to Ru. Examples of the $[Ru(bpy)_2(bpy(aeg_2))]^{2+}$ (i.e. Ru-hairpins), complexes **Ru-1** through **Ru-5**, are shown in Fig. 11.

Because of the synthetic requirements to make these complexes, new synthetic methodologies to produce these compounds in solution and to increase peptide length, coupling efficiency, and collected material yields were reported [71]. Higher coupling yields (30–60%) enabled isolation of product in gram scale quantities. The Ru compounds were characterized by a battery of methods including UV–vis absorbance spectroscopy, fluorescence spectroscopy, excited state transient decay, electrochemistry, and mass spectrometry. Comparison of the excited state lifetimes, extinction coefficients, quantum yields, and electrochemical properties revealed only minor variations between the series of Ru complexes.

Complexes **Ru-1**–**Ru-5** all contained free bipyridine ligands that were available for metal coordination. Addition of Cu^{2+} or Zn^{2+} resulted in formation of $[M(bpy)_2]^{2+}$ complexes pendant from the $[Ru(bpy)_3]^{2+}$ bridge, crosslinking the aeg strands. Incorporation of the acetyl spacer units in the aeg strands (Fig. 11) increased the distance between Ru and the coordinated metal. In complexes **Ru-4** and **Ru-5**, addition of a second set of bpy ligands allowed for complexation of a second metal ion.

4.5.3. Coordination of Cu to bpy-substituted aeg Ru-hairpins

Because $[Cu(bpy)_2]^{2+}$ is a known $[Ru(bpy)_3]^{2+}$ emission quencher, a series of emission titrations were performed with

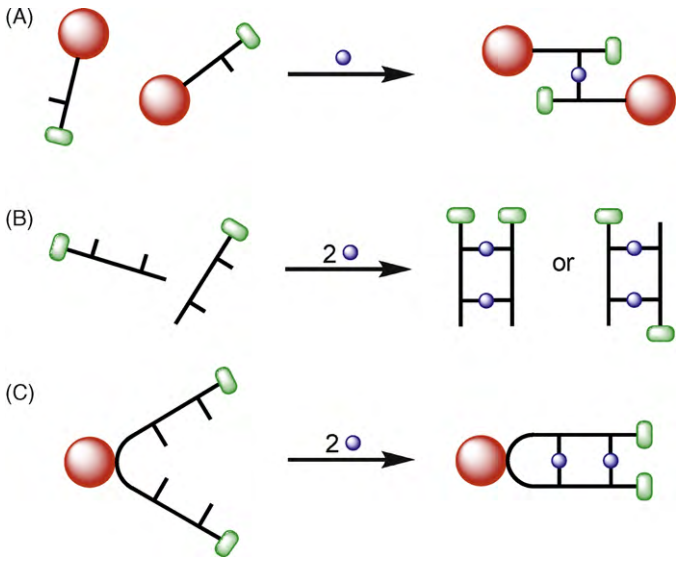

Fig. 12. Cartoon representation of binding motifs in ligand-substituted aeg strands. (A) Singe-stranded $Ru(bpy)_3^{2+}$ complexes crosslinked by the addition of Cu^{2+}. (B) Bpy dipeptide duplex forms parallel and antiparallel isomers when coordinating two Cu^{2+} ions. (C) Ru-hairpin motif prevents isomer formation; Cu^{2+} binding crosslinks strands.

known amounts of the Ru-hairpin complex. As Cu^{2+} was titrated into a solution containing the Ru complex, the emission intensity of $[Ru(bpy)_3]^{2+}$ decreased until it reached a minimum value and then leveled off. Fig. 13 shows a plot of the peak emission intensity (at 650 nm) as a function of the molar ratio of Cu to Ru. In the cases of **Ru-1**, **Ru-2**, and **Ru-3**, the emission intensity steadily decreased and then leveled at a ratio of ~1:1 Cu:Ru, as shown in Fig. 13A. At the equivalence point, the quenching efficiencies were 97, 95, and 90%, for **Ru-1**, **Ru-2**, and **Ru-3**, respectively, likely reflecting the increased distance between $[Ru(bpy)_3]^{2+}$, and the quencher $[Cu(bpy)_2]^{2+}$.

Compounds **Ru-4** and **Ru-5** contain two sets of free bpy ligands and as such were capable of coordinating two Cu^{2+} metal centers. Identical titration experiments were performed and the emission intensities as a function of the molar ratio of Cu to Ru were plotted; shown in Fig. 13B, the emission intensity decreased in two distinct stages. The shapes of these titration curves were attributed to two bound $[Cu(bpy)_2]^{2+}$ sites within the aeg scaffolds. After 2 equiv. of Cu are added to either **Ru-4** or **Ru-5**, their emission intensity decreased to 97%, equivalent to **Ru-1(Cu)**. This was expected since the distance between Ru and the nearest set of bpy ligands was roughly identical and thus the emission quenching efficiency should be approximately equal.

Elemental analysis confirmed the Ru:Cu ratios for all compounds. Shown in Fig. 14 for **$[Ru\text{-}5(Cu)_2]^{6+}$**, mass spectrometry was also used to conclusively determine the identity of the major species by analysis and comparison to calculated isotope splitting models. In all cases, multiple molecular ion peaks were observed in the mass spectra, corresponding to species with varying numbers of associated PF_6^- counteranions.

4.5.4. Quenching mechanism in Cu-linked Ru aeg hairpins

Excited state quenching of $[Ru(bpy)_3]^{2+}$ by $[Cu(bpy)_2]^{2+}$ can mechanistically occur by either electron or energy transfer, or a combination of these. Using the excited state redox potentials, electron transfer between the $bpy^{-\bullet}$ and Cu^{II} to form the $[Ru^{III}(bpy)_3]^{3+}$ and $[Cu^{I}(bpy)_2]^{1+}$ species has a calculated driving force of $\Delta G \approx -0.7$ eV. However, because $[Cu(bpy)_2]^{2+}$ has a weak, broad absorbance band that directly overlaps with the emission band of $[Ru(bpy)_3]^{2+}$, determination of the extent of energy transfer quenching remains difficult. To ultimately enable the use of these structures for molecular electronics applications, it is important to study and understand the interplay between structure, redox properties, and quenching mechanism.

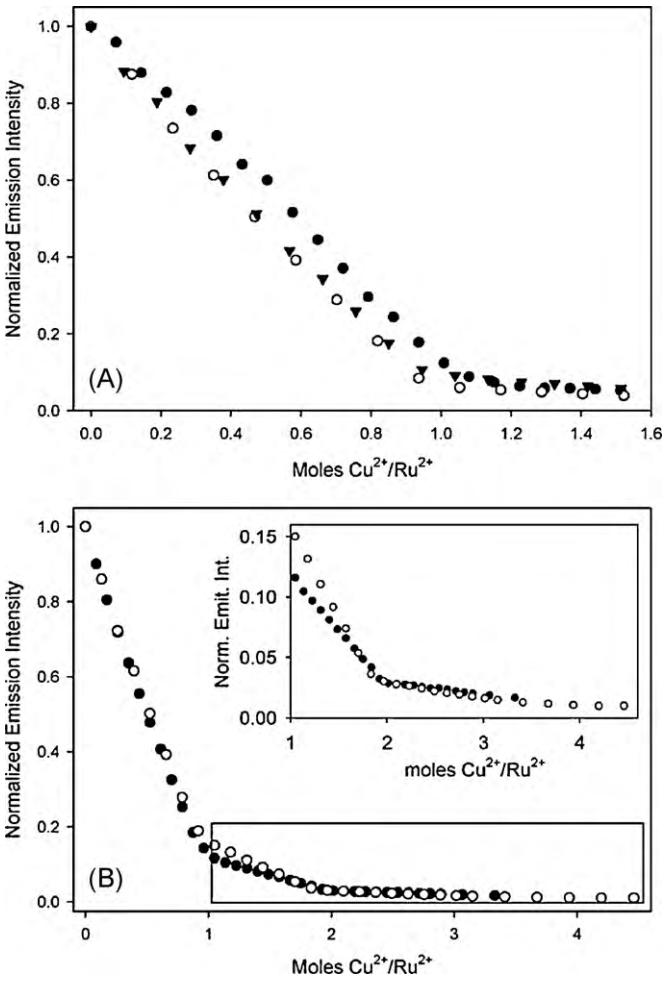

Fig. 13. (A) Plot of emission intensity of CH_3CN solutions containing (●) 140 μM **Ru-1** with addition of 5 μL aliquots of 5.3 mM $Cu(NO_3)_2$; (○) 58.7 μM **Ru-2** with additions of 5 μL aliquots of 3.41 mM $Cu(NO_3)_2$; (▼) 104 μM **Ru-3** with additions of 5 μL aliquots of 4.86 mM $Cu(NO_3)_2$. (B) Plot of emission intensity of CH_3CN solutions of (●) 95.0 μM **Ru-4** and (○) 57.6 μM **Ru-5** after incremental additions of 7 μL of 2.83 mM $Cu(NO_3)_2$ and 5 μL of 3.86×10^{-3} mM $Cu(NO_3)_2$, respectively, versus the molar ratio of Cu^{2+} to Ru^{2+}. (Inset) Expanded region of the titration curve at higher Cu^{2+} concentrations. Reproduced with permission from Ref. [71]. Copyright (2009) the American Chemical Society.

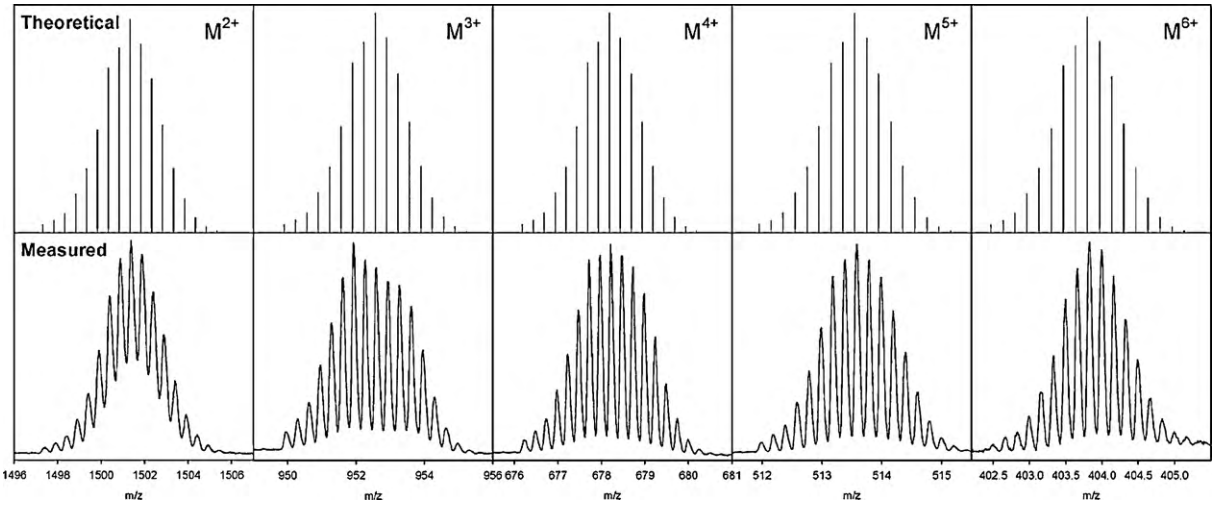

Fig. 14. Molecular ion peaks observed by positive ion electrospray mass spectrometry, plotted together with the calculated mass and isotopic splitting patters for $[Ru\text{–}5(Cu)_2](PF_6)_6$. Reproduced with permission from Ref. [71]. Copyright (2009) the American Chemical Society.

By measuring the excited state lifetimes of Ru–Cu systems, dynamics as a function of distance and number of Cu centers and as a function of temperature were obtained. Together with the quantum yields and temperature-dependent measurements, the non-radiative (k_{nr}) rates and activation energies (E_a) were calculated and compared. As the distance between Ru and Cu increased, k_{nr} decreased and E_a increased. In the cases of **Ru-4(Cu)$_2$** and **Ru-5(Cu)$_2$**, which each contained two $[Cu(bpy)_2]^{2+}$ complexes, these had k_{nr} and E_a values similar to **Ru-1(Cu)**, which was expected because the Ru–Cu distances are the same in the three compounds. Ongoing experiments aim to better understand the quenching mechanisms in these compounds.

5. Conclusions

This review has focused on a body of work that has used artificial peptide scaffolds to tether redox species together. Oligolysine and oligoproline strands containing electron donors, acceptors and chromophores are the seminal examples of coupling multifunctional systems to peptides. Because these formed helical structures, electron transfer distances were well controlled. Building on these examples, modification of double-stranded PNA duplexes to contain metallobases as coordinative crosslinks has been investigated. Most recently, architectures that assemble without the use of natural nucleobases or hydrogen bonding have been studied. Several of these also form double-stranded duplexes in solution by metal coordination chemistry to result in redox-active, multifunctional arrays. In total, these examples illustrate systems inspired by nature to tackle challenging problems in supramolecular self-assembly with potential applications in electron transfer.

Acknowledgments

The authors gratefully acknowledge the Division of Chemical Sciences, Geosciences, and Biosciences, Office of Basic Energy Sciences of the U.S. Department of Energy through grant (DE-FG02-08ER15986) for funding the development of the artificial oligopeptides for photoinduced electron transfer, and a grant from the National Science Foundation Chemistry Division (CHE-0718373) for supporting the development of inorganic molecular-recognition assembly of artificial oligopeptide duplexes.

References

[1] M.R. Wasielewski, J. Org. Chem. 71 (2006) 5051.
[2] M.R. Wasielewski, Chem. Rev. 92 (1992) 435.
[3] F.D. Lewis, R.L. Letsinger, M.R. Wasielewski, Acc. Chem. Res. 34 (2001) 159.
[4] T.J. Meyer, Acc. Chem. Res. 22 (1989) 163.
[5] J.H. Alstrum-Acevedo, M.K. Brennaman, T.J. Meyer, Inorg. Chem. 44 (2005) 6802.
[6] M.H.V. Huynh, T.J. Meyer, Chem. Rev. 107 (2007) 5004.
[7] R. Lomoth, A. Magnuson, M. Sjodin, P. Huang, S. Styring, L. Hammarstrom, Photosynth. Rev. 87 (2006) 25.
[8] N. Martin, L. Sanchez, B. Illescas, I. Perez, Chem. Rev. 98 (1998) 2527.
[9] R.V. Slone, J.T. Hupp, C.L. Stern, T.E. Albrecht-Schmitt, Inorg. Chem. 35 (1996) 4096.
[10] S.J. Lee, K.L. Mulfort, J.L. O'Donnel, X. Zuo, A.J. Goshe, P.J. Wesson, S.T. Nguyen, J.T. Hupp, D.M. Tiede, Chem. Commun. (2006) 4581.
[11] S.J. Lee, K.L. Mulfort, X. Zuo, A.J. Goshe, P.J. Wesson, S.T. Nguyen, J.T. Hupp, D.M. Tiede, J. Am. Chem. Soc. 130 (2008) 836.
[12] R.F. Kelley, S.J. Lee, T.M. Wilson, Y. Nakamura, D. Tiede, A. Osuka, J.T. Hupp, M.R. Wasielewski, J. Am. Chem. Soc. 130 (2008) 4277.
[13] R.A. Jensen, R.F. Kelley, S.J. Lee, M.R. Wasielewski, J.T. Hupp, D.M. Tiede, Chem. Commun. 16 (2008) 1886.
[14] P.J. Stang, D.H. Cao, J. Am. Chem. Soc. 116 (1994) 4981.
[15] P.J. Stang, B. Olenyuk, Organometallics 16 (1997) 3094.
[16] M.J.E. Resendiz, J.C. Noveron, H. Disteldorf, S. Fischer, P.J. Stang, Org. Lett. 6 (2004) 651.
[17] S.R. Seidel, P.J. Stang, Acc. Chem. Res. 35 (2002) 972.
[18] B.H. Northrop, Y.R. Zheng, K.W. Chi, P.J. Stang, Acc. Chem. Res. 42 (2009) 1554.
[19] K. Tanaka, M.J. Shionoya, Org. Chem. 64 (1999) 5002.
[20] K. Tanaka, Y. Yamada, M. Shionoya, J. Am. Chem. Soc. 124 (2002) 8802.
[21] K. Tanaka, A. Tengeigi, T. Kato, N. Toyama, M. Shiro, M. Shionoya, J. Am. Chem. Soc. 124 (2002) 12494.
[22] K. Tanaka, A. Tengeiji, T. Kato, N. Toyama, M. Shionoya, Science 299 (2003) 1212.
[23] Y. Takezawa, W. Maeda, K. Tanaka, M. Shionoya, Angew. Chem. Int. Ed. 48 (2009) 1081.
[24] E. Meggers, P.L. Holland, W.B. Tolman, F.E. Romesberg, P.G. Schultz, J. Am. Chem. Soc. 122 (2000) 10714.
[25] S. Atwell, E. Meggers, G. Spraggon, P.G. Schultz, J. Am. Chem. Soc. 123 (2001) 12364.
[26] N. Zimmermann, E. Meggers, P.G. Schultz, J. Am. Chem. Soc. 124 (2002) 13684.
[27] L. Zhang, E. Meggers, J. Am. Chem. Soc. 127 (2005) 74.
[28] S. Boyde, G.F. Strouse, W.E. Jones, T.J. Meyer, J. Am. Chem. Soc. 111 (1989) 7448.
[29] P. Chen, R. Duesing, G. Tapolsky, T.J. Meyer, J. Am. Chem. Soc. 111 (1989) 8305.
[30] W.E. Jones, C.A. Bignozzi, P. Chen, T.J. Meyer, Inorg. Chem. 32 (1993) 1167.
[31] K.A. Opperman, S.L. Mecklenburg, T.J. Meyer, Inorg. Chem. 33 (1994) 5295.
[32] S.L. Mecklenburg, D.G. McCaffety, J.R. Schoonover, B.M. Peek, B.W. Erickson, T.J. Meyer, Inorg. Chem. 33 (1994) 2974.
[33] S.L. Mecklenburg, B.M. Peek, B.W. Erickson, T.J. Meyer, J. Am. Chem. Soc. 113 (1991) 8540.
[34] S.L. Mecklenburg, B.M. Peek, J.R. Schoonover, D.G. McCafferty, C.G. Wall, B.W. Erickson, T.J. Meyer, J. Am. Chem. Soc. 115 (1993) 5479.
[35] D.G. McCafferty, B.M. Bishop, C.G. Wall, S.G. Hughes, S.L. Mecklenberg, T.J. Meyer, B.W. Erickson, Tetrahedron 51 (1995) 1093.
[36] D.G. McCafferty, D.A. Friesen, E. Danielson, C.G. Wall, M.J. Saderholm, B.W. Erickson, T.J. Meyer, Proc. Natl. Sci. Acad. U.S.A. 93 (1996) 8200.
[37] C.A. Slate, R.A. Binstead, T.J. Meyer, B.W. Erickson, Lett. Pept. Sci. 6 (1999) 61.
[38] C.A. Slate, D.R. Striplin, J.A. Moss, P. Chen, B.W. Erickson, T.J. Meyer, J. Am. Chem. Soc. 120 (1998) 4885.
[39] D.R. Striplin, S.Y. Reece, D.G. McCafferty, C.G. Wall, D.A. Friesen, B.W. Erickson, T.J. Meyer, J. Am. Chem. Soc. 126 (2004) 5282.
[40] P. Siders, R.A. Marcus, J. Am. Chem. Soc. 103 (1981) 748.
[41] S.A. Serron, W.S. Aldridge, C.N. Fleming, R.M. Danell, M.H. Baik, M. Sykora, D.M. Dattelbaum, T.J. Meyer, J. Am. Chem. Soc. 126 (2004) 14506.
[42] R.A. Marcus, Annu. Rev. Phys. Chem. 15 (1964) 155.
[43] N. Sutin, Prog. Inorg. Chem. 30 (1983) 441.
[44] R.A. Marcus, P. Siddarth, in: E. Kochanski (Ed.), Photoprocesses in Transition Metal Complexes, Biosystems and Other Molecules, Kluwer Academic Publishers, Netherlands, 1992.
[45] P.E. Nielsen, M. Egholm, R.H. Berg, O. Buchardt, Science 254 (1991) 1497.
[46] P.E. Nielsen, G. Haaima, Chem. Soc. Rev. 26 (1997) 73.
[47] H. Rasmussen, J.S. Kastrup, J.N. Nielsen, J.M. Nielsen, P.E. Nielsen, Nat. Struct. Biol. 4 (1997) 98.
[48] D.R. van Staveren, E. Bothe, T. Weyhermuller, N. Metzler-Nolte, Eur. J. Inorg. Chem. 6 (2002) 1518.
[49] A. Maurer, H.B. Kraatz, N. Metzler-Nolte, Eur. J. Inorg. Chem. 16 (2005) 3207.
[50] S.D. Koster, J. Dittrich, G. Gasser, N. Husken, I.C.H. Castaneda, J.L. Jios, C.O. Della Vedova, N. Metzler-Nolte, Organometallics 27 (2008) 6326.
[51] N. Husken, G. Gasser, S.D. Koster, N. Metzler-Nolte, Bioconjug. Chem. 20 (2009) 1578.
[52] D.L. Popescu, T.J. Parolin, C. Achim, J. Am. Chem. Soc. 125 (2003) 6354.
[53] R.M. Watson, Y.A. Skorik, G.K. Patra, C. Achim, J. Am. Chem. Soc. 127 (2005) 14628.
[54] R.M. Franzini, R.M. Watson, G.K. Patra, R.M. Breece, D.L. Tierney, M.P. Hendrich, C. Achim, Inorg. Chem. 45 (2006) 9798.
[55] A. Paul, R.M. Watson, P. Lund, Y. Xing, K. Burke, Y. He, E. Borguet, C. Achim, D.H. Waldeck, J. Phys. Chem. C 112 (2008) 7233.
[56] R.A. Marcus, J. Chem. Phys. 24 (1956) 966.
[57] R.A. Marcus, J. Chem. Phys. 43 (1965) 979.
[58] J.C. Genereux, J.K. Barton, Chem. Rev. doi:10.1021/cr900228f.
[59] S. Delaney, J.K. Barton, J. Org. Chem. 68 (2003) 6475.
[60] C.R. Treadway, M.G. Hill, J.K. Barton, Chem. Phys. 281 (2002) 409.
[61] F.D. Lewis, Pure Appl. Chem. 78 (2006) 2287.
[62] N.L. Frank, T.J. Meade, Inorg. Chem. 42 (2003) 1039.
[63] P. Wang, J.E. Miller, L.M. Henling, C.L. Stern, N.L. Frank, A.L. Eckermann, T.J. Meade, Inorg. Chem. 46 (2007) 9853.
[64] B.P. Gilmartin, K. Ohr, R.L. McLaughlin, R. Koerner, M.E. Williams, J. Am. Chem. Soc. 127 (2005) 9546.
[65] K. Ohr, B.P. Gilmartin, M.E. Williams, Inorg. Chem. 44 (2005) 7876.
[66] B.P. Gilmartin, R.L. McLaughlin, M.E. Williams, Chem. Mater. 17 (2005) 5446.
[67] K. Ohr, R.L. McLaughlin, M.E. Williams, Inorg. Chem. 46 (2007) 965.
[68] C.P. Myers, B.P. Gilmartin, M.E. Williams, Inorg. Chem. 47 (2008) 6738.
[69] L.A. Levine, H. Youm, H.P. Yennawar, M.E. Williams, Eur. J. Inorg. Chem. (2008) 4083.
[70] L.A. Levine, S.I. Kirin, C.P. Myers, S.A. Showalter, M.E. Williams, Eur. J. Inorg. Chem. (2009) 613.
[71] C.P. Myers, J.R. Miller, M.E. Williams, J. Am. Chem. Soc. 131 (2009) 15291.
[72] K. Kalyanasundaram, Coord. Chem. Rev. 46 (1982) 159.
[73] S. Fukuzumi, Eur. J. Inorg. Chem. 9 (2008) 1351.
[74] C.W. Cady, R.H. Crabtree, G.W. Brudvig, Coord. Chem. Rev. 252 (2008) 444.
[75] M. Falkenstrom, O. Johansson, L. Hammarstrom, Inorg. Chim. Acta 360 (2007) 741.